Applied Catalysis B: Environmental 231 (2018) 137–150

Contents lists available at ScienceDirect

Applied Catalysis B: Environmental

journal homepage: www.elsevier.com/locate/apcatb

Natural solar light-driven preparation of plasmonic resonance-based alloy and core-shell catalyst for sustainable enhanced hydrogen production: Green approach and characterization

Mandari Kotesh Kumar*, Jeong Yeon Do, Police Anil Kumar Reddy, Misook Kang*

Department of Chemistry, College of Natural Sciences, Yeungnam University, 280 Daehak-Ro, Gyeongsan, Gyeongbuk 38541, Republic of Korea

ARTICLE INFO

Keywords:
Bi metallic
Alloy
Core-shell
Hydrogen production
Titania nano particles

ABSTRACT

Plasmonic Co and/or Ag monometal and their combinations as bimetal alloy and core-shell nanoparticles were prepared under natural sun light, using aqueous glycerol (in-situ reducing agent) and TNP (stabilizer). The formation of bimetallic alloy and core-shell NPs, and their uniform dispersion on the surface of TNP were evidenced by different characterization techniques. Ultraviolet-visible diffuse reflectance spectroscopy evidenced the two distinct characteristic surface plasmon resonance (SPR) absorption bands for the core-shell nanoparticles and a single distinct characteristic SPR band for the alloy. X-ray photoelectron spectroscopy revealed the presence of Ag and Co in the metallic form. The results of H_2-temperature programmed reduction of fresh and used samples emphasized the characteristic reduction peaks for the reduction of monometal/bimetal oxide to metallic/bimetallic particles. The interaction of the loaded bimetallic particles with TNP resulted in a shift in the Raman bands. The photoluminescence spectra of the used samples revealed the formation of bimetallic alloy and core-shell structures, which resulted in a decrease in the recombination of charge carriers. X-ray diffraction, electron paramagnetic resonance spectroscopy, high-resolution transmission electron microscopy, and cyclic voltammetry analyses substantiated the same. The monometal-loaded photocatalysts and the bimetal alloy and core-shell nanoparticle-loaded photocatalysts were further examined for H_2 production with pure water/aqueous glycerol/crude glycerol under natural solar light irradiation. The $(Ag\text{-}Co)_{coloaded}$TNP catalyst yielded the maximum H_2 evolution rate of 63 mmol g^{-1}. For comparison, experiments were conducted under artificial solar light irradiation with similar experimental conditions. Based on the results, different mechanistic paths for insitu photoreduced Ag-Co bimetallic alloy and core-shell nanoparticles on TNP for H_2 production are envisaged.

1. Introduction

Energy poverty caused by huge amount of combustible fossil burning has resulted in an ambitious search for other energy resources, which are both environmentally friendly and renewable [1]. Since the discovery of the phenomenon of H_2 production from water on a TiO_2 photocatalyst in the 1970s [2], it has drawn significant attention owing to its promising applications [3]. However, as a typical largeband gap (3.2 eV) semiconductor, it has a high recombination rate of photo-induced e^- and h^+ pairs, and its primary absorbance in the UV spectrum range severely hinders its practical applications under solar radiation. Different methods have been adopted for enhancing the catalytic activity of TiO_2 by doping with various noble and transition monometal and bimetal elements such as impregnation, sol-gel, and photodeposition. Supported bimetallic catalysts have drawn much attention because of their tunable and synergistic effects compared to monometallic counterparts [4], which can form either alloys or core-shell structures. Alloys and core-shell materials have attracted much attention because of their unique physicochemical properties, and are useful in photonics, electronics, and catalysis. When monometal particles were used for photocatalytic H_2 production, the particles also acted as the active sites for hydrogen evolution reaction (HER) [5]. However, as an electronsink and HER catalyst, monometal particles have a much lower activity than the bimetal particles do. Thus, to attain high efficiency for photocatalytic H_2 production, bimetal alloy and/or core-shell particles are desirable as they combine the advantages of both the localized surface plasmon resonance (LSPR) effect and activation effect of alloy and core-shell particles.

Alloy and core-shell nanoparticles (NPs) also exhibit great potential in photocatalysis;however, only a few relevant studies can be found in

* Corresponding authors.
E-mail addresses: koteshkumar@ynu.ac.kr (K.K. Mandari), mskang@ynu.ac.kr (M. Kang).

https://doi.org/10.1016/j.apcatb.2018.03.015
Received 10 July 2017; Received in revised form 14 February 2018; Accepted 5 March 2018
Available online 06 March 2018
0926-3373/

literature. Various bimetallic alloy and core-shell NPs have been reported such as AuPd/$BiVO_4$ [6], Au-Ag alloy NPs-coated TiO_2 [7], Au-Pd/GR alloy [8], Co@CoO core-shell nanocrystals [9], and Ag_2S-5%/Ag_3PO_4 core/shell composites [10], which exhibit superior activity than their corresponding monometallic NPs do. Watanabe et al. reported AgCo nanostructures embedded in TiO_2 thin films fabricated by pulsed laser deposition, wherein the size and density of the Ag-Co hybrid nanostructures were controlled during film growth [11]. Ag and Co bimetallic alloy [12] and core-shell NPs [13–22] strongly absorb visible light because of the LSPR [23] derived from the collective oscillation of conductive electrons. The LSPR-enhanced strong local electric field near the particle surface gives rise to the surface-enhanced Raman scattering and infrared absorption effects [24]. In addition, the LSPR-induced strong local electric field increases the activity of the semiconductor photocatalysts and serves as an electron sink, retarding the recombination of photo-generated charge carriers in TiO_2.

To the best of our knowledge, only afew reports exist on Ag-Co alloy and core-shell NPs loaded on TNP for enhanced H_2 production under natural sun light. For the preparation of Ag-Co alloy and core-shell NPs, two metallic precursors were added simultaneously in the one-pot co-reduction method. In this case, the metal's reduction potentials play a key role in determining the final architecture. Two possibilities arise here: (i) metals with similar reduction potentials are reduced simultaneously and form an alloy structure and (ii) metals with different reduction potentials are reduced in a successive manner and form a core-shell structure. However, there is no straightforward relationship between reduction potential and reduction kinetics. The reduction kinetics also depends on the synthesis conditions. For example, the use of surfactants, stronger reducing agents (such as $NaBH_4$), or high-temperature solvothermal processes can lead to simultaneous reduction of metals with different reduction potentials resulting in an alloy structure [25–28]. Alongside the wet impregnation procedures, much attention has been paid to colloidal chemistry to synthesize unsupported NPs with controlled shape, size, and stability [29]. While colloidal chemistry is highly applicable to the synthesis of noble metal bimetallic systems, its application in transition 3d metals is less studied.

A notable SPR mode exists whose energy is concentrated at the interface between the core and shell, which we call the extraordinary SPR mode. In addition, the conventional SPR mode, whose energy is concentrated at the outer surface of the bimetallic NP, is called the ordinary SPR mode. The ordinary and extraordinary SPR modes together determine the line shape of the extinction spectrum as well as the shift of the SPR peak (to shorter or longer wavelengths) as a function of different geometric parameters [30]. Further control of the LSPR frequency in a wider range has been achieved by either alloy or core-shell bimetallic NPs. The interaction of the two metallic components in either nanometer or atomic scale permits facile tuning of the surface plasmon band mostly in solution phases. The resulting LSPR frequency in general lies in between those of the pure components, depending on the relative amounts of the two components.

The novelty of this study is that the catalysts were prepared by in-situ photoreduction of Ag/Co bimetallic core-shell and alloy NPs (utilizing natural sun light as the energy source) and their loading onto TNP (as stabilizer) by using glycerol (as a scavenger/reducing agent). Co/Ag bimetallic core-shell and alloy catalysts produced maximum amount of hydrogen than the monometallic catalysts did under solar light irradiation. The surface plasmon behavior of the bimetallic core-shell and alloy photocatalysts were investigated by using H_2 temperature-programmed reduction (H_2-TPR), powder X-ray diffraction (XRD), ultraviolet-visible diffuse reflectance spectroscopy (UV-DRS), X-ray photoelectron spectroscopy (XPS), high-resolution transmission electron microscopy (HRTEM), and photoluminescence (PL) spectroscopy. Thus, in the present report, we have identified the different combinations of Ag and Co bimetallic core-shell and alloy NPs for improved catalytic H_2 evolution through electron sink catalytic properties of Co and Ag, respectively, and the beneficial properties of TiO_2 NPs.

2. Experimental

2.1. Materials and reagents

Analytical grade titanium isopropoxide ($Ti[OCH(CH_3)_2]_4$), glycerol, cobalt nitrate, and silver nitrate (AR grade) were obtained from Sigma Aldrich. Acetic acid (CH_3COOH), ammonia (NH_3) solution, and ethanol (EtOH) were procured from Ranchem Ltd., South Korea.

2.2. Preparation of TNP

TNP were prepared by the sol-gel method. In a typical procedure, the two solutions were prepared independently in a 250 mL beaker. Solution-A was prepared by dissolving 3 mL of acetic acid in 36 mL of EtOH, and solution-B was prepared by dissolving 4 mL of $Ti(OC_3H_7)_4$ in 36 mL of EtOH. Solution-A was added dropwise to solution-B under vigorous stirring and aged for 4 h, following which a transparent gel was obtained. At this stage, an aqueous NH_3 solution was added slowly under vigorous stirring and continued until a precipitate was obtained. The resulting solid was not subjected to further washing with water/solvent and was dried at 80 °C in an oven for 12 h, followed by calcination in air at 450 °C for 4 h at the rate of 5 °C/min.

2.3. Preparation of monometallic and bimetallic catalysts

Monometallic (different wt% metals) CoTNP and AgTNP, and three bimetallic catalysts, Co_{loaded}-AgTNP, Ag_{loaded}-CoTNP, and $(Ag\text{-}Co)_{coloaded}$TNP, were synthesized (Scheme S0) by the impregnation method. For the preparation of bimetallic catalysts (best optimized metal combination is Ag (1 wt%) and Co (2 wt%)), 1 g of TNP was added to 10 mL deionized water to which required amounts of $Co(NO_3)_2{\cdot}6H_2O$ and/or $Ag(NO_3)_2{\cdot}6H_2O$ aqueous salt solutions were added. The suspension was stirred until the solvent completely evaporated and then dried at 80 °C for about 12 h and calcined at 450 °C at 4 °C/min for 5 h. Co_{loaded}-AgTNP and Ag_{loaded}-CoTNP samples were prepared by the different loading order of Co and Ag. In the first case, Co (2 wt%) was loaded onto the surface of pre-synthesized 1 wt %AgTNP and named as Co_{loaded}-AgTNP, whereas in the second case, Ag (1 wt%) was added to pre-synthesized 2 wt%CoTNP and named as Ag_{loaded}-CoTNP. The $(Ag\text{-}Co)_{coloaded}$TNP sample was prepared by adding simultaneously the aqueous solutions of cobalt nitrate (2 wt %Co) and silver nitrate (1 wt% Ag) to pre-synthesized TNP. After complete screening of several combinations (metal loadings on TNP) and conducting experiments for hydrogen production, hereafter, the 1 wt%Ag-loaded TNP was named as AgTNP and 2 wt%Co-loaded TNP was named as CoTNP.

2.4. Characterization of photocatalysts

The XRD patterns of the photocatalysts were recorded on a PANalytical X-ray diffractometer using Ni-filtered Cu K_α radiation (λ = 1.5406 Å) ranging from 2θ = 10 to 80° with a scan rate of 10°/min and beam voltage and beam current of 30 kV and 30 mA, respectively. The surface area was measured by N_2 physical adsorption at −196 °C using a BELSORP-mini II (BEL-Japan Inc., Japan) instrument. The specific surface area was calculated according to the BET method. For TEM and HRTEM analyses, samples were dispersed in the EtOH solution and suspended on a 3.5-mm-diameter Cu grid of 400-mesh, and images were taken using an H-7600 (Hitachi, Japan) HRTEM accelerated with 120 kV. For structural characterization, the Raman spectra of the samples were recorded on a Horiba Jobin-Yvon lab ram HR spectrometer using a λ = 632.81 nm laser beam excitation. The infrared spectra were measured in the range of 4000–400 cm^{-1} with a Nicolet is10 (ThermoFisher) scientific spectrometer. The UV–vis DR spectra were recorded at room temperature using a Neosys-2000 (scinco co. Korea) spectrophotometer equipped with a diffuse

reflectance attachment with $BaSO_4$ as a reference standard in the range of 185–800 nm, and the spectra were converted to the Kubelka–Munk function. The XPS patterns were recorded using a Kratos Axis Ultra Imaging equipped with aMg anode and a multi channel detector. Charge referencing was done against adventitious carbon (C 1s, 284.7 eV), and a Shirley-type background was subtracted from the signals. The calculated spectra were fitted using Gauss-Lorentz curves to determine the BE of the different elements. EPR spectra were recorded on a JEOL/JES-FA200 EPR spectrometer at room temperature using the X-band equipment with an operating frequency of $\upsilon = 9.029$ GHz. TPR analysis was measured in a quartz reactor interfaced to a GC-TCD unit. Hydrogen consumption was calculated by analyzing the effluent gas using a calibration curve of TPR of Ag_2O under a similar protocol. The PL spectra of the catalysts were measured by using a spectrofluorometer (FLUORA MAX 4P) at 330 nm exciton wavelength. SEM (SEM, HITACHI S-4800) equipped with an energy dispersive X-ray (EDX) unit was used for surface morphology, microstructural, and elemental characterizations. The CV results were recorded using a BAS 100B electrochemical analyzer at a scan rate of 100 mV/s with 0.1 M KCl as the supporting electrolyte, a platinum wire as the working and counter electrodes, and Ag/AgCl as the reference electrode. The FTIR spectra of the samples were recorded in the range of 4000–400 cm^{-1} at ambient temperature using an Agilent Cary 600 FTIR spectrometer.

2.5. Evaluation of photocatalytic activity

The photocatalytic H_2 evaluation experiments were conducted as reported in our previous publications [31,32]. To evaluate the stability of the photocatalyst, recycle study was carried out for 5 cycles. The 1st cycle of the experiment was carried out as indicated in the above procedure for 20 h under light irradiation. After completion of the 1st cycle, the reactor was kept overnight in dark with air tightly at room temperature. Prior to the 2nd cycle, the gas products were evacuated, and the reactor was purged with N_2 gas and analyzed by GC to ensure the absence of H_2. The same study was repeated for the 3rd, 4th, and 5th cycles of the experiment.

3. Results anddiscussion

3.1. X-ray diffraction (XRD)

The crystalline structures of fresh and post-reaction laboratory-made TNP and Co and/or Ag (mono/bimetal)-loaded TNP photocatalysts were examined by XRD, and the XRD profiles of the freshly prepared mono/bimetal-loaded TNP are depicted in Fig. S1 and Table 1. The post-reaction/used photocatalysts exhibited a similar XRD pattern as that of the freshly prepared ones (Fig. S1), suggesting minor

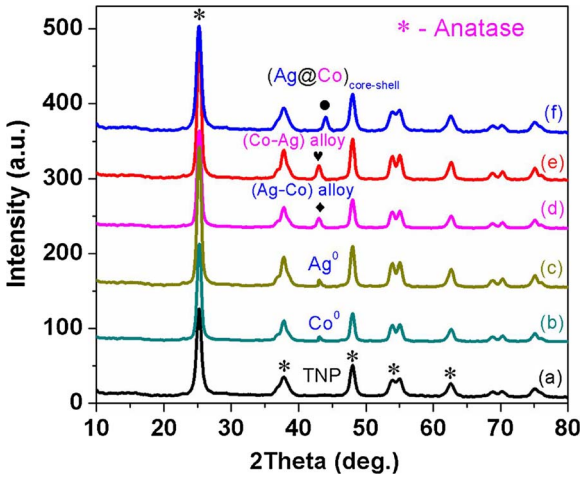

Fig. 1. XRD patterns of post-reaction/used samples: (a) TNP, (b) CoTNP, (c) AgTNP, (d) Ag_{loaded}-CoTNP, (e) Co_{loaded}-AgTNP, and (f) $(Ag\text{-}Co)_{coloaded}$TNP.

changes in the crystallite size and intensity of the post-reaction/used samples. All the diffraction peaks of the post-reaction/used (Fig. 1) CoTNP, AgTNP, Ag_{loaded}-CoTNP, Co_{loaded}-AgTNP, and $(Ag\text{-}Co)_{coloaded}$TNP samples exhibited no shift compared with that of TNP, indicating that Co and Ag were not incorporated into the lattice of TNP but instead were well dispersed and loaded on the surface of TNP [33]. However, no diffraction peaks of metal oxide species were observed in the XRD profile of the fresh catalysts (Fig. S1), which indicated that they are finely dispersed and that the metal content is less than 5 wt%; therefore, it is very difficult to identify these metal oxides, which is the limitation of XRD [34]. In contrast, in the post-reaction/used samples, an additional diffraction peak at 43.2° was observed in the profiles of CoTNP, AgTNP, Ag_{loaded}-CoTNP, and Co_{loaded}-AgTNP, indicating the formation of metallic Co°, Ag°, Ag-Co alloy, and Co-Ag alloy in the NPs (Fig. 1). Furthermore, compared to Co°, Ag°, Ag-Co alloy and Co-Ag alloy peaks, $(Ag\text{-}Co)_{core\text{-}shell}$ has a larger crystallite size and the diffraction peak $2\theta = 44.1°$ shifted to a higher diffraction angle, which is due to the formation of core-shell structure in the post-reaction/used $(Ag\text{-}Co)_{coloaded}$TNP sample. To confirm the state of $(Ag\text{-}Co)_{core\text{-}shell}$ on the surface of TNP in $(Ag\text{-}Co)_{coloaded}$TNP, $(Ag\text{-}Co)_{core\text{-}shell}$ was further characterized by UV–vis DRS, HRTEM, and XPS.

A well-defined XRD pattern can be clearly seen, with peaks corresponding to fcc Ag alone. However, peaks or bands corresponding to neither metallic Co nor Co oxides were observed. These results agree with the results of bimetallics reported by Garcia-Bastida et al. in the sense that no Bragg reflections for Co were detected [35]. In another report on bimetallic core-shell NPs, dealing with nanoparticles of

Table 1
Physicochemical characteristics of the mono (CoTNP, AgTNP) and bimetallic Co/Ag loaded photocatalysts.

Photocatalyst	BET Surface area ($m^2\,g^{-1}$)	Band gap (eV)[a]		Crystallite size (nm)[b] (Anatase TiO_2)	H_2 uptake ($\mu mol/g_{cat}$)		% Photo reduction
		Fresh	Photo reduced		[c]Fresh	[d]Photo reduced	[e]H_2-TPR (bulk)
TNP	79.5	3.20	3.20	14.1	nd	nd	nd
CoTNP	72.1	2.89	2.75	14.0	160.9	76.1	44.6
AgTNP	71.4	2.84	2.72	13.9	233.0	132.4	46.6
Co_{loaded}-AgTNP	62.9	2.80	2.60	13.7	584.5	261.3	51.2
Ag_{loaded}-CoTNP	62.4	2.79	2.58	13.7	580.8	271.6	52.7
$(Ag\text{-}Co)_{coloaded}$TNP	60.8	2.74	2.49	13.4	598.7	297.5	54.9

nd: not determined.
[a] Measured from UV-DRS.
[b] Measured from XRD spectra using Debye–Scherrer formula.
[c] H_2 uptakes of fresh calcined catalysts measured by H_2-TPR with a calibrated Ag_2O TPR.
[d] H_2 uptakes of the used catalysts measured by H_2-TPR.
[e] Extent of bulk photo reduction of the catalysts measured from H_2 uptakes of the fresh and used catalysts (c and d).

higher size was reported the presence of both Co and Ag reflections [36] of the dissimilar particle sizes could explain the observed results. Moreover, it has been reported that the absence of Bragg reflections of the metal core in XRD could be indicative of a correct core-shell formation [37,38]. A similar observation has been reported that in core-shell NPs, in which the heavier metal forms the shell, only the peaks of the heavier metal are observed in the XRD pattern [39]. The formation of Co and/or Ag alloy (Fig. 1) was observed when the sequential impregnation method was adopted for Ag_{loaded}-CoTNP and Co_{loaded}-AgTNP samples. A similar XRD pattern was observed for the formation of Co/Ag alloy by different groups [17,40]. Further, the surface area of the samples slightly decreased with an increase in the metal loading, which can be mainly ascribed to the loaded particles that are blocking the surface of TNP (Table 1).

3.2. UV-DRS absorption spectroscopy

The UV–vis absorption spectra of freshly prepared CoTNP, AgTNP, Ag_{loaded}-CoTNP, Co_{loaded}-AgTNP, and $(Ag\text{-}Co)_{coloaded}$TNP photocatalysts are displayed in Fig. S2. Compared to TNP, the absorption edges of mono/bi metal-loaded TNP photocatalysts were shifted toward longer wavelengths (Fig. S2b–f), which is attributed to a decrease in the band gap of the freshly prepared photocatalysts. Freshly prepared metallic photocatalysts show progressive visible-light absorption. Zhou et al. [41] reported that Ag_2O/TiO_2 (Fig. S2) catalysts showed absorption in the visible region beyond 390 nm due to the increased number of electronic states in the surface lattice by the interaction of Ag^+ ions with TiO_2. In contrast, the absorption spectra of CoTNP (Fig. S2) showed a gradual shift of the absorption edge toward longer wavelengths [42]. The band edges (Fig. S2) of the bimetallic photocatalyst spectra shifted toward the red region as compared to that of the monometallic absorption spectra. Moreover, it was found that with increase in metal content, the absorption edges of the samples shifted toward longer wavelengths and the band gap values of the photocatalysts decreased.

It was reported that the DRS spectra of Co-doped TiO_2 showed a red shift (Fig. S2) in the absorption value. Increase in the concentration of Co ions on TiO_2 resulted in a prominent change or shift of the band edge from the UV to visible region [42]. The estimated band gap energy (E_g) values are listed in Table 1 (calculated using the formula $E_g = 1240/\lambda$). Obviously, with the metal content, the E_g decreased in CoTNP, AgTNP, Ag_{loaded}-CoTNP, Co_{loaded}-AgTNP, and $(Ag\text{-}Co)_{coloaded}$TNP (Fig. S2). With decrease in band gap energy, the yield of the photo-generated electron-hole pair may increase, which is more favorable for the photocatalytic activities of Ag_{loaded}-CoTNP, Co_{loaded}-AgTNP, and $(Ag\text{-}Co)_{coloaded}$TNP than those of TNP, AgTNP, and CoTNP.

3.3. H_2-temperature-programmed reduction (H_2-TPR)

The H_2-TPR profiles of the freshly prepared and post-reaction/used CoTNP, AgTNP, Ag_{loaded}-CoTNP, Co_{loaded}-AgTNP, and $(Ag\text{-}Co)_{coloaded}$TNP photocatalyst samples are presented in Fig. 2. AgTNP shows a single reduction peak centered at 137 °C, which is assigned to the reduction of Ag^+ ions to metallic Ag. The low-temperature reduction signal is attributed to the finely dispersed Ag particles. In contrast, the TPR profile of CoTNP displayed two reduction peaks at ca. 341–455 and 457–663 °C, which correspond to the reduction of Co_3O_4 to CoO and CoO to Co metal, respectively [43–45] and can be attributed to the reduction of Co^{2+} interacting with TNP. Moreover, the peak at 421 °C in CoTNP could be related to the reduction of isolated Co, and the peak at 645 °C could be attributed to the strong interaction between Co and TNP [46]. The H_2-TPR profiles of Ag_{loaded}-CoTNP, Co_{loaded}-AgTNP, and $(Ag\text{-}Co)_{coloaded}$TNP exhibited three reduction peaks. The first reduction peak at 141 °C was attributed to the reduction of Ag oxide to metallic Ag, and the second and third reduction peaks were attributed to the reduction of Co^{3+} to Co^{2+} and Co^{2+} to Co°, respectively [44,47].

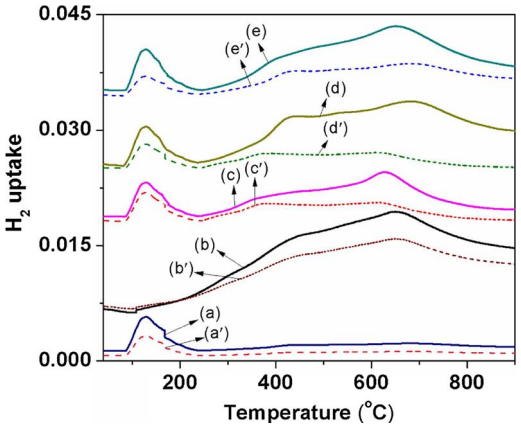

Fig. 2. TPR profiles of fresh samples of (a) AgTNP, (b) CoTNP, (c) Ag_{loaded}-CoTNP, (d) Co_{loaded}-AgTNP, and (e) $(Ag\text{-}Co)_{coloaded}$TNP and post-reaction/used samples of (a') AgTNP, (b') CoTNP, (c') Ag_{loaded}-CoTNP, (d') Co_{loaded}-AgTNP, and (e') $(Ag\text{-}Co)_{coloaded}$TNP.

Compared to the Ag_{loaded}-CoTNP reduction peaks, the Co reduction peaks of Co_{loaded}-AgTNP and $(Ag\text{-}Co)_{coloaded}$TNP shifted to high-temperature regions. The post-reaction/used samples also exhibited similar reduction profiles as that of the freshly prepared catalysts, with peaks at ~138 °C, 340–450, and 450–660 °C, which can be attributed to the reduction of Ag_2O to Ag°, Co_3O_4 to CoO, and CoO to Co, respectively. The reduction peak intensities of post-reaction/used photocatalysts were lower than those of the freshly prepared photocatalysts. The T_{max} of these reduction signals and the H_2 uptakes were significantly low, which suggest the partial reduction of metal oxide to metal during photocatalytic reaction under illuminated conditions. The extent of photoreduction during the course of reaction was estimated from the H_2-TPR analysis of freshly prepared calcined samples and post-reaction/used catalysts, and their corresponding H_2 uptakes are reported in Table 1. The results imply that the reduction process had already occurred to some extent during the course of the reaction and that parts of Ag_2O and cobalt oxide were insitu photoreduced and transformed into metallic, alloy, and core-shell species.

3.4. PL spectroscopy

The PL spectra of the freshly prepared samples indicated a strong luminescent material with an emission band observed at 410 nm, which is ascribed to active electron-hole recombination (Fig. 3A). As the intensity of TNP is higher than that of CoTNP, AgTNP, Ag_{loaded}-CoTNP, Co_{loaded}-AgTNP, and $(Ag\text{-}Co)_{coloaded}$TNP, it leads to the spatial separation of electron-hole pairs and effectively prevents them from recombination. PL spectral analysis provides information on the electronic transition behavior of the materials; alloy and core-shell Ag-Co NPs effectively accept the excitons from the TNP support and improve the lifetime of charge carriers on the semiconductor surfaces during the catalytic process. In addition, the particles seem to promote the separation of photo-induced charge carriers (e^- and h^+) resulting from electronic transitions on the catalyst surface. These surface species mainly originate from the surface defects and surface oxygen vacancies and their energy levels are localized between the valence and conduction bands of the semiconductors. They can significantly influence the photo-induced charge behavior to modify the semiconductor performance. These factors are possibly responsible for the increase in surface oxygen vacancy and defect content, which in turn decrease the PL intensity of the freshly prepared samples. In the case of post-reaction/used CoTNP, AgTNP, Ag_{loaded}-CoTNP, Co_{loaded}-AgTNP, and $(Ag\text{-}Co)_{coloaded}$TNP samples (Fig. 3B), the respective monometal and the bimetal alloy and core-shell NPs come in contact with TNP leading to the formation of a Schottky junction. However, we ascribe the decrease in emission intensity to severe quenching by metal particles deposited

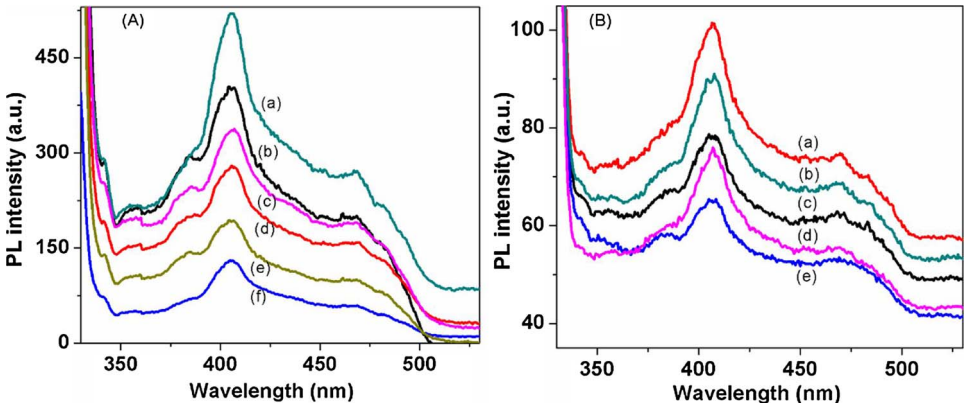

Fig. 3. PL spectra of (A) freshly prepared samples (a) TNP, (b) CoTNP, (c) AgTNP, (d) Ag_{loaded}-CoTNP, (e) Co_{loaded}-AgTNP, and (f) $(Ag\text{-}Co)_{coloaded}$TNP and (B) post-reaction/used samples (a) CoTNP, (b) AgTNP, (c) Ag_{loaded}-CoTNP, (d) Co_{loaded}-AgTNP, and (e) $(Ag\text{-}Co)_{coloaded}$TNP.

on titania [17,48].

Thus, the formation of a Schottky junction helps not only in the separation of photo-generated charge carriers, but also in the effective suppression of photo-generated electron-hole recombination. The PL intensity of the post-reaction/used $(Ag\text{-}Co)_{coloaded}$TNP is a result of the reduction in electron-hole recombination caused by the formation of Schottky junction in the core-shell semiconductor [13]. The charge recombination in $(Ag\text{-}Co)_{coloaded}$TNP is less than that in AgTNP and CoTNP. However, after photo-treatment, when these two metals combined to form core-shell particles in $(Ag\text{-}Co)_{coloaded}$TNP, the coexistence of Co and Ag in the bimetal core-shell favored further reduction of electron-hole recombination. Therefore, the weaker PL emission observed for the bimetal catalysts could be ascribed to the lesser photogeneration of electron-hole pairs in TNP due to the shade of incident light by the Ag@Co core-shell NPs and the suppressed electron-hole recombination since the excess Ag@Co core-shell NPs on the surface of TNP would prevent visible-light absorption by TNP.

3.5. Electron paramagnetic resonance (EPR)

Fig. 4A and B show the EPR spectra of monometal and bimetal-loaded freshly prepared and post-reaction/used catalysts. Freshly prepared TNP did not show any EPR signal, whereas the fresh and used monometal and bimetal-loaded TNP catalysts exhibited paramagnetic signal, which is attributed to the presence of Ag^+ and Co^{2+} ions on the surface of TNP. The Ag^+ and Co^{2+} ions separated and coordinated with the oxygen ion located at the surface of TNP, which are susceptible to photoreduction. The spectrum is characterized by a strong EPR signal, which is normally the result of high-spin Co^{2+} ions on the surface of TiO_2 [49]. The EPR peak intensities of the post-reaction/used catalysts were lower than that of the freshly prepared catalysts. It may be noted that the presence of Ag°, Co°, bimetal alloy, and core-shell NPs may disturb the EPR results to some extent by electrically absorbing visible intensity and thus decreasing the total EPR intensity of the used sample. The analysis of surface electron capture in the presence of Ag°, Co°, bimetal alloy, and core-shell-loaded TNP could provide a reasonable idea of the electron/hole trapping capability of the sample at the surface as well as the behavior of such charge carriers under photo-irradiated conditions.

3.6. Raman spectroscopic analysis

The Raman spectra of freshly prepared photocatalyst samples are shown in Fig. 5. The laboratory-prepared TNP exhibited only the anatase phase, with peaks (Fig. 5a) corresponding to the anatase phase at 149 (E_g), 205 (E_g), 397 (B_{1g}), 512 (B_{1g}), and 635 cm^{-1} (E_g) [50]. The E_g mode arises due to the vibration of oxygen atoms in the O—Ti—O bonds, while the B_{1g} and A_{1g} modes correspond to the symmetric and anti-symmetric bending vibrations of the O—Ti—O bonds, respectively. The Raman peaks of CoTNP, AgTNP, Ag_{loaded}-CoTNP, Co_{loaded}-AgTNP, and $(Ag\text{-}Co)_{coloaded}$TNP samples shifted to higher wavenumbers as compared to those of the TNP (Fig. 5b–f). It has been established from the Raman spectral study of freshly prepared catalysts that the intensity, shape, and position of the Raman peaks are strongly affected by the phonon confinement effect, defects, lattice strain, and crystallite size and shape. Moreover, the spectra shows that the Raman peaks of monometal loadings shifted toward higher energies, while that of the bimetal loadings on TNP shifted toward lower energies (Fig. 5 inset). The significant differences in peak intensity, peak broadening, and peak shift confirm the structural and morphological differences caused by

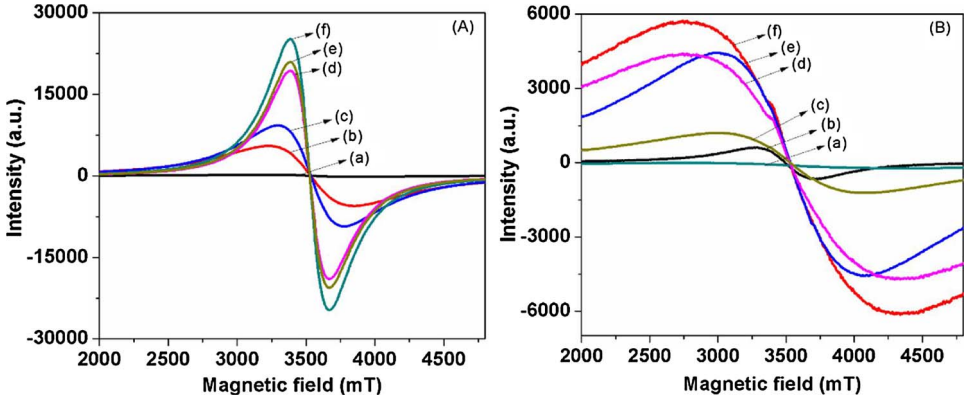

Fig. 4. EPR spectra of (A) freshly prepared samples (a) TNP, (b) CoTNP, (c) AgTNP, (d) Ag_{loaded}-CoTNP, (e) Co_{loaded}-AgTNP, and (f) $(Ag\text{-}Co)_{coloaded}$TNP and (B) post-reaction/used samples (a) TNP, (b) CoTNP, (c) AgTNP, (d) Ag_{loaded}-CoTNP, (e) Co_{loaded}-AgTNP, and (f) $(Ag\text{-}Co)_{coloaded}$TNP.

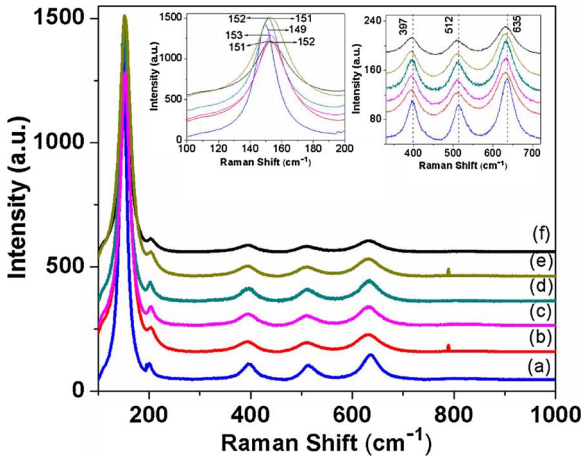

Fig. 5. Raman spectra of freshly prepared samples: (a) TNP, (b) CoTNP, (c) AgTNP, (d) Ag_{loaded}-CoTNP, (e) Co_{loaded}-AgTNP, and (f) $(Ag\text{-}Co)_{coloaded}$TNP.

the loading of Co and/or Ag and Co/Ag on TNP [51–53]. In the present study, shifts caused by metal loading indicate an alteration in oxygen stoichiometry or a higher concentration of oxygen vacancies in the monometal and bimetal catalyst particles. Such oxygen vacancies are assumed to be the preferential adsorption sites for glycerol as well as for water splitting on the surface of TNP.

3.7. X-ray photoelectron spectroscopy (XPS)

The surface oxidation states of mono/bimetallic NP materials were analyzed by XPS. The XPS spectra of O1s, Ti2p, Cu2p, and Ag3d of the freshly prepared and post-reaction/used Ag_{loaded}-CoTNP, Co_{loaded}-AgTNP, and $(Ag\text{-}Co)_{coloaded}$TNP samples are depicted in Fig. 6. The O 1s peak appearing at BE ~530.1 eV corresponds to surface oxygen from the hydroxyl group on TNP. The Ti 2p spectra shows two well resolved intense peaks at 459.7 eV and 464.9 eV corresponding to Ti $2p_{3/2}$ and Ti $2p_{1/2}$, respectively, indicating the presence of Ti^{4+}. In bimetal samples, the peaks at 780.6 eV and 796.7 eV are attributed to Co $2p_{3/2}$ and Co $2p_{1/2}$, respectively, which are assigned to CoO. The presence of shakeup satellites at 785.8 and 803.7 eV (Fig. 6) may indicate that the oxidation state of Co is +2 [54]. The Co BEs of the post-reaction/used catalysts are slightly shifted toward lower BEs, i.e., (780.1 and 795.7 eV); (780.2 and 795.8 eV); (780.0 and 795.6 eV), compared to that of the freshly prepared catalysts, which indicates the presence of metallic Co in the bimetal alloy and core-shell structure.

For a cobalt titania catalyst, the Co $2p_{3/2}$ and Co $2p_{1/2}$ peaks appeared at 780.00 and 795.13 eV, indicating that Co is in a reduced state [55]. Moreover, it was reported that in a post-reaction Co-loaded titania catalyst, the Co $2p_{3/2}$ and Co $2p_{1/2}$ peaks appeared at 780.05 and 795.20 eV, respectively, indicating that the cobalt oxidation state changed to +2 and then to 0 after several hours of reaction under UV light irradiation. We obtained similar results in this study, i.e., Co $2p_{1/2}$ shows two main peaks located at 793.4 and 795.5 eV, in which the peak at BE = 793.4 eV fits well with that reported for metallic Co, while the peak at BE = 795.5 eV agrees with Co(II) in the form of CoO. In addition, two intense satellites were located at the higher BE side of the main peaks, which are characteristic of the CoO spectra [56,57]. Thus, the present XPS result confirms the Co to be zero valent since it has been reported that unlike gold and silver, zero-valent Co nanometal is very sensitive to air and moisture, which renders the stabilization of Co NPs in aqueous medium challenging [58].

In the Ag spectra, the BE values of (368.0 and 373.8 eV); (368.0 and 373.8 eV); and (367.9 and 373.7 eV) are assigned to $Ag3d_{5/2}$ and $Ag3d_{3/2}$ of Ag_2O of the freshly prepared Ag_{doped}-CoTNP, Co_{doped}-AgTNP, and $(Ag\text{-}Co)_{codoped}$TNP catalysts, respectively, while in the Ag 3d spectra of used Ag_{doped}-CoTNP, Co_{doped}-AgTNP, and $(Ag\text{-}Co)_{codoped}$TNP catalysts, the BE of (367.2 and 372.9 eV); (367.0 and 372.8 eV); (366.9 and 372.5 eV) could be attributed to metallic Ag. These BE values are lower than those reported for bulk metallic Ag (Ag $3d_{5/2}$ = 368.1, Ag $3d_{3/2}$ = 374 eV) [59]. Although the BE for the oxides ((Ag_2O = $3d_{5/2}$ = 367.3 eV) and (Ag_2O = $3d_{5/2}$) = 367.7 eV)) (Hoflund et al.) fits better than that of the metallic Ag, the existence of silver oxides is discarded. Moreover, a shift in the Ag 3d peaks with respect to that of pure Ag was observed due to a different chemical environment; this is because the Co core could modify the energy levels, resulting in a different BE [60].

The BEs of Ag in the bimetal alloy and core-shell catalysts were slightly shifted from the corresponding BEs of the fresh samples, confirming that Ag is in the metallic (Ag°) form. This shift suggested that charge transfer occurred from Ag to Co and Co to Ag, which was caused by the difference between the work functions of Ag (4.26 eV) and Co (5.0 eV) [15]. More importantly, the BE of the bimetal core-shell catalyst shifted toward a lower energy level with respect to that of the bimetal alloy. It was presumed that these phenomena occurred because the charge transfer in the core-shell structures differed from that in the alloyed structures. Similar results were reported, that is, the BEs of the metallic Ag° state (Ag $3d_{5/2}$) for a $Ag@Co_3O_4$ core-shell and Ag-Co alloy shifted to lower values (367.5 and 368.0 eV, respectively) compared to that of the pure Ag (368.2 eV). This negative shift suggested that charge transfer occurred from Ag to Co_3O_4 (or Co), which was caused by the difference between the work functions of Ag (4.26 eV) and Co_3O_4 (4.5 eV) (or Co (5.0 eV)). In another report, more importantly, the BE of the $Ag@Co_3O_4$ core-shell shifted to a higher energy level with respect to that of the Ag-Co alloy. It was presumed that these phenomena occurred because the charge transfer in the core-shell structures differed from that in the alloyed structures [15]. Ha et al. reported that metallic Co° (18.2%) was only observable for the Ag-Co alloy. Thus, it was inferred that the metallic Co on the surface of the Ag-Co alloy nanocrystals partially transformed into CoO and subsequently to the Co_3O_4 phase, which was thermodynamically favored [61]. It was found that oxygen vacancies on the surface of the $Ag@Co_3O_4$ core-shell (76.7%) and Ag-Co alloy (83.0%) were more abundant than on pure Ag (53.0%) and Co_3O_4 (27.7%). Thus, it could be postulated that charge transfer from Ag to Co_3O_4 (or Co) may contribute to the formation of enriched oxygen vacancy defects by the generation of oxygen anions [62]. The spectra revealed that the d-band center of the $Ag@Co_3O_4$ core-shell hybrid (4.16 eV) and Ag-Co alloy nanocrystals (4.49 eV) shifted upward compared to that of Ag nanocrystals (4.77 eV) [63].

4. Discussion

4.1. Study of photocatalytic activity for H_2production

4.1.1. Activity of crystalline anatase TiO_2 NPs

TNP (laboratory-made TiO_2 NP photocatalyst) is a highly active photocatalyst owing to its wide band gap energy of ~3.20 eV (Table 1), and gets activated in the UV region. Under natural solar light (~ only 5% UV radiation), TNP demonstrates a minimal H_2 evolution rate (409 μmol g^{-1}). Using a solar simulator (artificial solar lamp), a lower rate (390 μmol g^{-1}) of hydrogen evolution is observed. The rate of hydrogen production in pure water is comparatively less due to the fast recombination of charge carriers ($e^- - h^+$). Therefore, in order to avoid fast recombination of charge carriers ($e^- - h^+$) in TNP (TiO_2), the photocatalyst is loaded with a co-catalyst such as Ag and/or Co individually and doped with bimetal to enhance the lifetime of charge carriers, and further experiments were conducted under natural solar light irradiation using aqueous glycerol .

4.1.2. Activity of Ag_2O-loaded crystalline anatase TNP

Fig. S6 displays the effect of different amounts (wt%) of Ag_2O loading on TNP for photocatalytic hydrogen evolution using aqueous glycerol mixture. When the doped Ag_2O concentration increased above

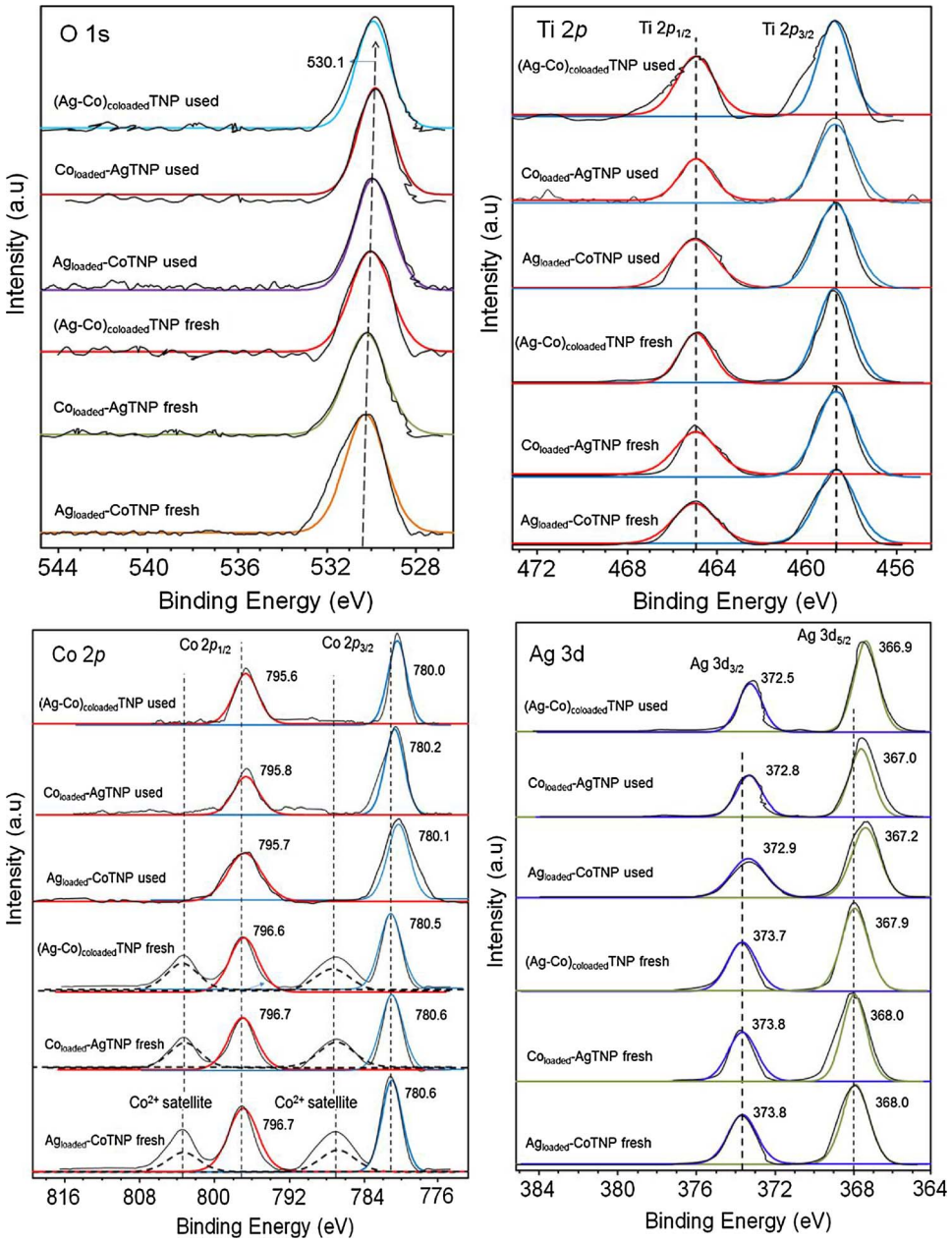

Fig. 6. XPS spectra of freshly prepared and post-reaction/used photocatalysts: (A) O 1s, (B) Ti 2p, (C) Co 2p, and (D) Ag 3d.

0.5 wt%, the photocatalytic activity increased gradually. The higher photocatalytic activity of Ag_2O-doped samples with increasing Ag_2O loading up to 1.0 wt% could be due to the improved dispersion of Ag_2O particles over the TNP photocatalyst. As 1.0 wt% Ag_2O is the optimum amount of Ag loading on TNP (as listed in Table 1, band gap = 2.84 eV), it resulted in light harvesting and a lower rate of electron-hole recombination. In addition, a higher amount of Ag (> 1.0 wt%) would cover more of the TNP surface and hinder the contact between TNP and organics (hole scavenger), which would increase the diffuse distance and decrease the amount of received photons [64–66], thereby decreasing the rate of hydrogen production, as clearly depicted in Fig. S6. In the present study, 1.0 wt% Ag_2O-loaded TNP exhibited a maximum of 31.3 mmol g^{-1} hydrogen production rate under the given set of experimental conditions under natural solar irradiation (Scheme 1). Therefore, after a certain period of reaction (16 h), the rate of hydrogen production on 1.0 wt% AgTNP gradually decreased (Fig. S6).

4.1.3. Activity of Co-loaded TNP

Based on the above results of Ag loading, TNP was modified with another cheaply available metal with a similar work function as that of Ag, i.e., Co, by adopting the wet impregnation method. The 1 wt% CoTNP photocatalyst showed ~29.9-fold enhancement in the H_2 production rate than that of TNP. As shown in Fig. S7, the hydrogen production rate increased (31.2 mmol g^{-1}) with increasing Co loading up to 2 wt%; above this loading, the activity decreased. The higher photocatalytic activity of the Co-loaded samples with increasing Co loading on TNP up to 2 wt% could be due to the improved dispersion of Co particles over the TNP photocatalyst. It was observed that at 2 wt% Co loading on TNP, the light harvesting as well as the lower electron-hole recombination is satisfied.

4.1.4. Activity of Ag-Co bimetal-loaded TNP

Bimetallic particles demonstrate unique catalytic activity and electronic and optical properties distinct from those of the corresponding metallic particles used in photonics, electronics, optics, and drug

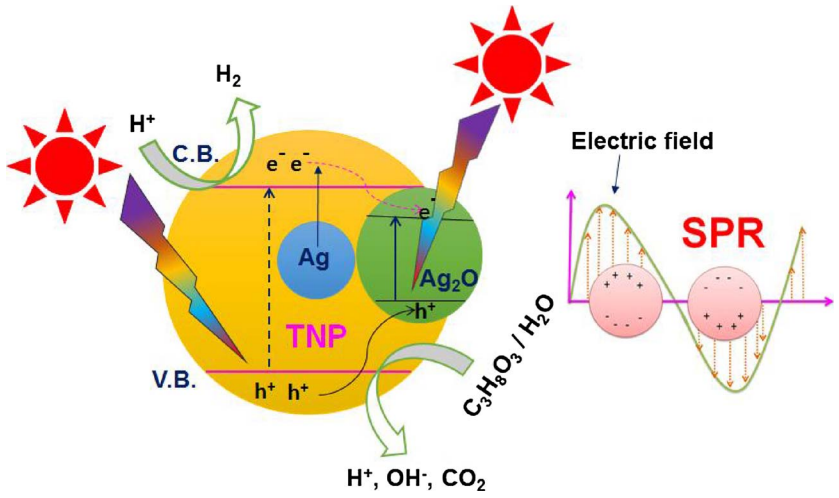

Scheme 1. Surface plasmon-mediated silver loaded on TNP for hydrogen production under natural solar light.

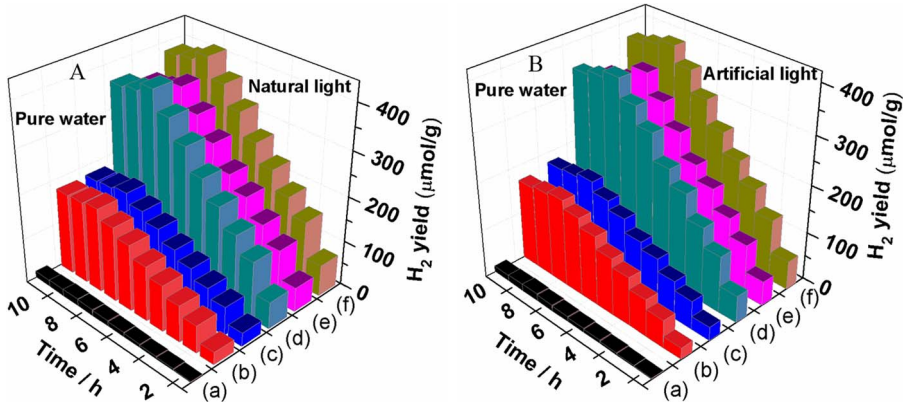

Fig. 7. Pure H_2O splitting activities over (a) TNP, (b) CoTNP, (c) AgTNP, (d) Co_{loaded}-AgTNP, (e) Ag_{loaded}-CoTNP, and (f) $(Ag\text{-}Co)_{coloaded}$TNP under (A) natural solar light and (B) artificial solar light. Water = 50 mL, catalyst ~10 mg.

delivery [13]. In this regard, the bimetal-loaded titania are expected to exhibit not only the combination of properties associated with the two distinct metals, but also new properties because of the synergy between the two metals. However, the improvement in photocatalytic activity of TiO_2 modified with non-noble metal particles by bimetallization. To further improve the hydrogen production activity, different combinations of both the metals (more economical than gold and platinum) were loaded on the TNP photocatalyst using the wet impregnating technique (Fig. 7).

The above experiments demonstrated that loading with either Ag or Co monometal induces the ability to absorb visible light due to LSPR (Fig. 8b and c), and the plasmon metals activate the wide-band gap semiconductors (TNP, i.e., TiO_2) toward visible light. However, loading with a single element could not meet the requirements for practical applications, and therefore, co-loading with different metals was attempted to achieve higher photocatalytic hydrogen production activity. The activity-promoting effect of bimetal is attributed to the improved spatial charge separation in TNP. It is well known that the work function of metal decreases upon alloying with other metal components with a lower work function, and it has been reported that alloying of Pt with other metals decreases the work function of Pt NPs. This may decrease the conduction band and promote efficient e^- transfer from NPs to the anatase semiconductor or charge carrier transfer from metal NPs to the conduction band of TiO_2 [67]. It is well known that surface plasmonic bands are characteristic for metal NPs [68]. Fig. 8 presents the UV–vis DRS absorption spectra of Co and/or Ag dispersion and that of loaded pure Ag and Co dispersions on TNP for comparison [69].

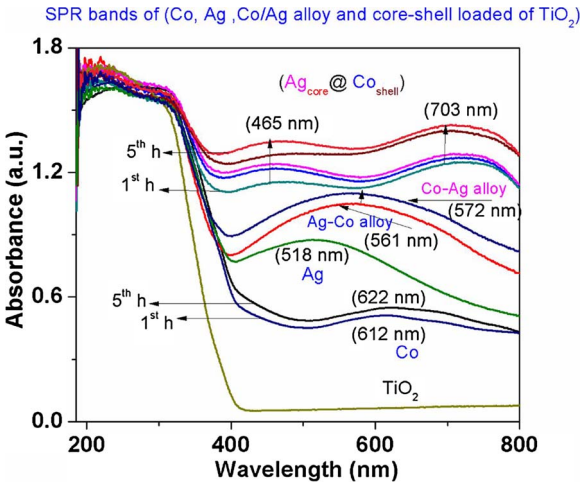

Fig. 8. UV-DRS spectra of post-reaction/used samples: (a) TNP, (b) CoTNP (1st h, 5th h), (c) AgTNP, (d) Ag_{loaded}-CoTNP, (e) Co_{loaded}-AgTNP, and (f) $(Ag\text{-}Co)_{coloaded}$TNP (1st h, 5th h).

The post-reaction Ag-loaded TNP photocatalyst exhibited a visible-light absorption peak at 518 nm corresponding to the surface plasmon resonance (SPR) band of metallic Ag, while Co-loaded TNP exhibited an absorption band at 612 nm corresponding to the SPR band of metallic Co particles. A similar plasmonic behavior of Ag and Co was observed and reported elsewhere [23,70,71]. In this study, after five hours of

photocatalytic hydrogen production reaction under natural sun light, it was noticed that the SPR band shifted to a higher wavelength (622 nm), which is attributed to the enhancement of metallic Co particles that reduced to metallic particles with different shape (Fig. 8b). The nature of bimetallic nanoparticles depends critically on their shape, size, structure, and composition, either as core-shell or alloy NPs. Ag_{loaded}-CoTNP and Co_{loaded}-AgTNP showed broad absorption bands at 562 nm and 572 nm, which are attributed to the SPR band of Ag-Co and Co-Ag alloy, respectively. This type of broad absorption band was not present in the case of monometal-loaded CoTNP, AgTNP, and $(Ag\text{-}Co)_{coloaded}$TNP. During the photocatalytic process, in Ag_{doped}-CoTNP, the Ag ions first underwent reduction followed by the reduction of Co, consequently forming Ag-Co alloy nanoparticles (NPs). In contrast, in Co_{doped}-AgTNP, the Co ions underwent photoreduction first, followed by the Ag ions. The bands in the UV-DRS spectra of the bimetal catalysts differed from the superposition of the DRS spectra of CoTNP and AgTNP, suggesting that some portions of Co and/or Ag species interacted with the TNP surface. The post-reaction/used samples (photoreduced) such as CoTNP and AgTNP (Fig. 8) exhibited SPR bands approximately at 612 nm and 518 nm, respectively. The distinct broad absorption bands due to the surface plasmon signals at 561 nm and 572 nm (Fig. 8) evidenced the formation of Co-Ag and Ag-Co alloy NPs, which is entirely different from the monometal (Co and/or Ag)-loaded TNP. The spectrum of $(Ag\text{-}Co)_{coloaded}$TNP shows absorption bands at 465 nm and 703 nm, which are attributed to the SPR bands of (Ag-Co) core-shell. Moreover, since this resonance is on the interface of the metal and support, these oscillations are very sensitive to metal-support interaction. In this case, the bands at 465 nm and 703 nm could be attributed to the resonance of (Ag-Co) core-shell NPs that strong interact with the support. It was reported that the appearance of a single SPR band [72] in the spectrum of NP suspensions depending on composition is in agreement with alloy formation, whereas well-defined geometries such as core-shell NPs gave rise to two SPR bands [73] corresponding to Ag and Au phases, respectively.

The formation of core-shell structure can be elucidated based on the insitu photoreduction effect of Co and Ag ions by photoirradiation treatment. When light energy was applied along the particles during the reaction, the Ag^+ ions were reduced on the surface of cobalt oxide and after cobalt oxide particles has also been reduced. It could be deduced that several Ag particles were covered by Co to form a core-shell structure. The intensity of SPR of the samples changed with irradiation time due to the reduction of metal oxide to metal over a period of illumination. The Ag_2O and CoO species underwent reduction with increase in irradiation time;as a result, the absorption bands appeared red-shifted. With increase in irradiation time, the rate of reduction of metal oxide to metal increased, consequently enhancing the SPR peak.

Based on the substantial data from the above photocatalytic experimental study of monometallic (2CoTNP and 1AgTNP) photocatalysts, the bimetallic photocatalytic activity for hydrogen production was examined by varying the combination of metals (Table 1 and Schemes 2 and 3). The bimetallic 1Ag-2CoTNP photocatalyst exhibited better photocatalytic activity with the aqueous glycerol mixture, as is shown in Fig. 9. The notable changes in the catalytic properties upon bimetal loading on TNP is caused by changes in the electronic properties of the particle by the formation of an active (formation of an alloy/core-shell of Ag and Co) surface structure of TNP. The rates of photocatalytic hydrogen production by monometal- and bimetal-loaded TNP under natural and artificial solar light irradiation were compared and the results are presented in Figs. S6 and S7 and , respectively. The rate of H_2 production using $(Ag\text{-}Co)_{coloaded}$TNP was 63 mmol g^{-1}, which is 65 and 2 times greater than that of pure TNP and monometal-loaded TNPs, respectively. This result evidences the synergistic effect of the two metals loaded on TNP [74].

The LSPR energy transfer from plasmon metal to the semiconductor takes place via two different mechanisms that is direct electron transfer (DET) and plasmon resonance energy transfer (PRET). Here the LSPR energy transfer occurs via DET mechanism when the metal and semiconductor are in direct contact and the PRET mechanism takes place while the metal and semiconductor are separated by a spacer layer that prevents the DET process. In the case of PRET, the strong electromagnetic field generated by the LSPR allows the transfer of energy. In the AgTNP or CoTNP, the Ag and Co metals are in direct contact with the TiO_2 surface and the SPR energy enhanced electron can directly transfer from the Ag or Co metal to the TiO_2 surface through this direct contact similar to the mechanism observed for the dye sensitization. However, in the case of the Ag_{loaded}-CoTNP, Co_{loaded}-AgTNP, and $(Ag\text{-}Co)_{coloaded}$TNP the SPR energy transfer follows the PRET mechanism. The Co particles in these bimetal composites acts as an insulating layer which prevents the direct contact of Ag nanoparticles with the TiO_2 surface. Hence the energy transfer takes place via the nonradiative PRET process form the LSPR dipole of Ag metal to the transition dipole of the TiO_2 semiconductor. In other words, the strong localized electromagnetic field of the LSPR of Ag metal can be relaxed by exciting an electron hole pair in the semiconductor without the emission of a photon.

The enhancement in activity when the metals were loaded individually may be attributed to the fact that loading of either Ag or Co results in the formation of Schottky barriers at the AgTNP and CoTNP contact regions, respectively, thus promoting the charge transfer and inhibiting the recombination of electron-hole pairs. The loadings of Ag and Co particles serve as electron sinks and decrease electron-hole recombination, and act as active sites for proton reduction, thereby increasing the production of H_2. As the loadings of Ag_2O and CoO increased, the crystallites become bulky and tend to demonstrate bulk characteristics such as absorption of shorter wavelengths and fast electron-hole recombination, resulting in a lower rate of hydrogen production.

The catalytic properties of bimetallic nanoparticles are directly related to their structure and composition, which may be controlled by the processes taking place during the reaction. It is clear from the experimental and characterization studies that the [15,20,23] Ag:Co ratio of 1:2 is better than the other combinations and appears (Fig. 9) optimum for the effective formation of core-shell/alloy NPs (HRTEM Fig. 10) and yielding the highest rate of hydrogen production under of the employed experimental conditions. It shows that the lattice fringe of 0.20 nm is consistent with (200) plane of Ag, while the lattice fringe of 0.21 nm is assigned to the (100) plane of Co. On the other hand, Co, Ag, O, and Ti elements were observed in the EDS spectra (Figs. 10 and S4) of bimetal catalysts. The photo-generated Ag and Co on TNP semiconductor surface can separately trap the reductive electrons and oxidative holes and prevent their combination, and then transfer these trapped electrons or holes to the absorbed substances on their surfaces. Under visible-light irradiation, the higher photocatalytic activity of 1Ag-2CoTNP NPs can be attributed to the shift in light absorbance and lowering of band gap (Table 1), as shown in the UV-DRS results, which increase their existent life and improve the efficiency of the photocatalytic reaction. The photocatalytic activity mainly depends on the catalyst architecture: Co-Ag particles with suitable size (nm), which are assumed to be located on anatase TNP, behave as active sites for the reaction. This photocatalysis is promoted via plasmon activation of the Co-Ag particles by visible light followed by consecutive electron transfer into the conduction band of anatase TNP. The activated Co-Ag particles transfer their conduction electrons to the adjacent anatase TiO_2. These catalyzes the oxidation of substrates (glycerol/water), producing protons and thus generated during oxidation and undergoes reduction of H^+ by the conduction band electrons on the surface of anatase TNP (TiO_2). This plasmonic photocatalysis is successfully promoted by sunlight exposure and enables efficient and selective oxidation of alcohol at ambient temperature.

On the other hand, bimetallic catalysts exhibit synergies including “ligand effect” and “ensemble effect” [75–77]. The former results from geometrical arrangement of surface atoms in a fashion appropriate for a

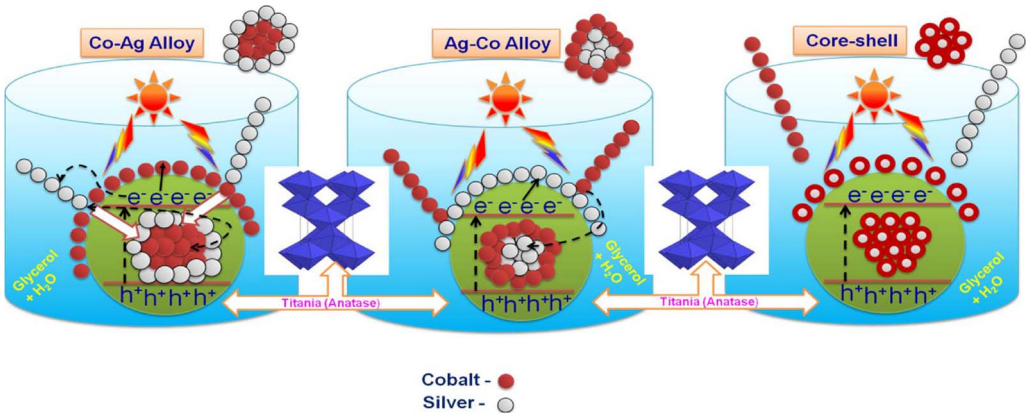

Scheme 2. Schematic representation of surface plasmon resonance of insitu-generated Ag-Co bimetallic alloy and core-shell NPs on TNP for hydrogen production under natural solar light.

particular reaction to occur, while the latter is induced by the modification of electronic state(s) of either or both the guest and host metals. Thus, bimetallic cluster-loaded TNP ($M_1 - M_2$/TNP) has the potential to achieve high photocatalytic activity through fine-tuning of the topology and/or the electronic state of the surface atoms. However, there are only a few studies on the photocatalysis of bimetal-loaded TiO_2 [78,79]. The electron charge transfer from M_1 to M_2 (or vice versa) can affect the adsorption property of the substrates. In addition, the photocatalytic water splitting activity of TNP can depend on the electron transfer from TNP to the substrate via M_1 and M_2. Particularly, in the core-shell-type bimetal, since the electron charge transfer is one-directional (vectorial), these effects would be enhanced.

4.1.5. Effect of bimetal catalyst sacrificial agents

Photocatalytic H_2 generation were conducted over various sacrificial agents with increasing carbon chain length C_1–C_3 and compared with crude glycerol and mono-, di-, and tri-hydroxylic alcohols in order to enhance the electron-hole recombination time;the results are shown in Fig. 11. It is well established that sacrificial agents can affect the photocatalytic activity of the catalyst. Hence, experiments were conducted on the optimized catalyst with methanol, ethanol, ethylene glycol, crude glycerol, and glycerol to learn the scavenger's role in improving the photocatalytic activity. Interestingly, the scavengers greatly influenced the activity in the order:crude glycerol < methanol < ethanol < ethylene glycol < glycerol. The tri-hydroxylic alcohols showed substantial hydrogen generation than the mono- and di-hydroxylic alcohols did due to the polarity of the alcohol, which strongly influences the surface properties such adsorption and electron donation properties of the catalysts [80]. The alcohols and carbohydrates effect of hole scavengers for photocatalytic hydrogen generation has also been reported [81]. It was reported that the H_2 evaluation rate depends on substrate polarity; the H_2 generation rate increased with increase in the polarity of alcohols in the order:glycerol > ethylene glycol > methanol > ethanol > iso-propanol [82–84].

Thus, for photocatalytic H_2 generation, a neutral condition is favorable, while acidic and basic conditions are unfavorable. This can be due to some reasons such as the effect of pH on the positions of the conduction and valence bands in the semiconductor and the semiconductor surface charge [85]. On the other hand, the adsorption of glycerol on catalyst may be another important issue that affects the photocatalytic reaction. The surface charge and surface acidity/basicity characteristics influence the adsorption of glycerol on TNP [86].

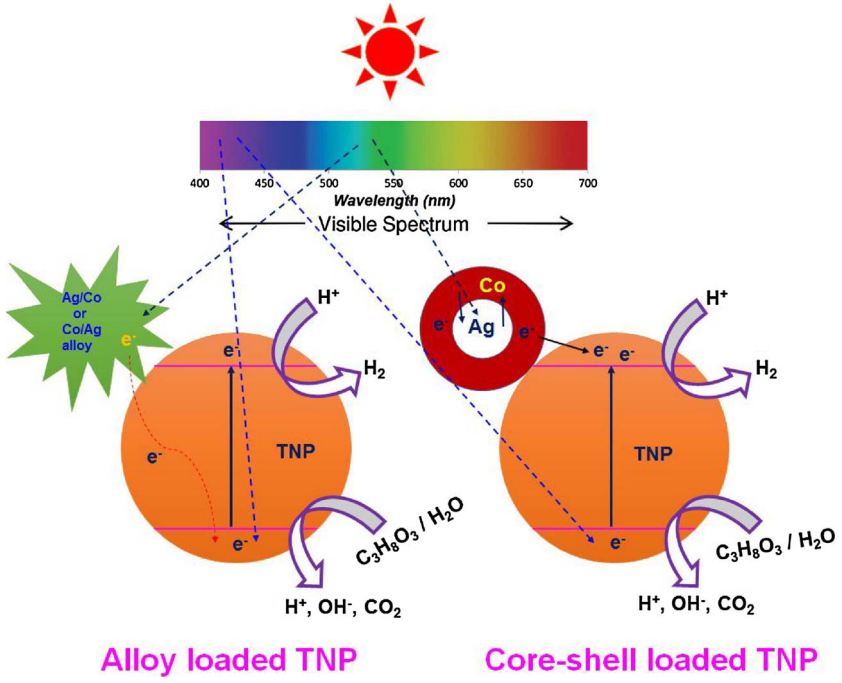

Scheme 3. Surface plasmon-mediated alloy and/or core-shell NPs loaded on TNP for hydrogen production under natural solar light.

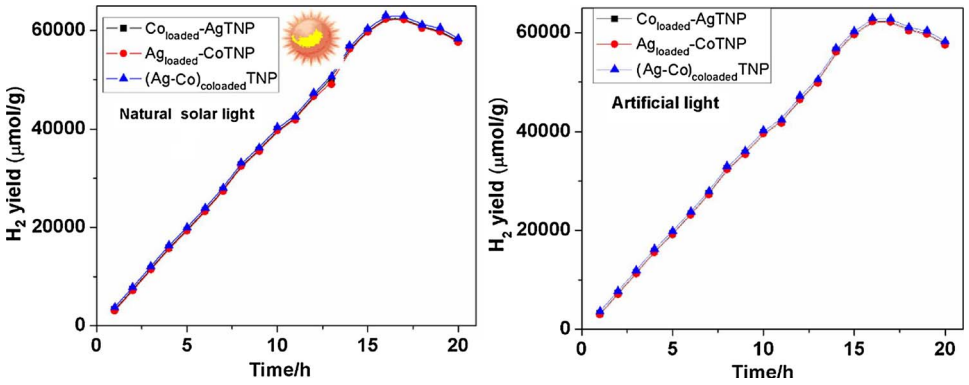

Fig. 9. Effect of different loadings of Ag_2O and CoO co-doped on TiO_2 for hydrogen production activity under natural and artificial solar light: (a) Co_{loaded}-AgTNP, (b) Ag_{loaded}-CoTNP, (c) $(Ag\text{-}Co)_{coloaded}$TNP (Reaction conditions: at ambient temperature, time = 20 h, sacrificial reagent = aqueous glycerol (10 vol%) solution, amount of photo catalyst: 10 mg).

4.1.6. Effect of bimetal catalyst amount

A series of experiments (Fig. 12) were carried out by varying the amount of catalyst from 5, 10, 15, and 20 mg in 50 mL of glycerol-water mixture with respect to different photocatalysts such as Ag_{loaded}-CoTNP, Co_{loaded}-AgTNP, and $(Ag\text{-}Co)_{coloaded}$TNP under both artificial and natural solar light irradiation. The best results were observed at the optimal catalyst amount of 10 mg in $(Ag\text{-}Co)_{coloaded}$TNP; below or above this loading, a lower rate of H_2 production was observed. Optimum hydrogen production rates of 62.9 mmol g^{-1} (artificial solar light) and 63 mmol g^{-1} in natural solar light were observed with ~0.1 g_{cat} h^{-1}. Catalyst loading above 10 mg could also be a disadvantage for photocatalytic H_2 generation since particle agglomeration can lead to increased turbidity of the colloidal dispersion, resulting in opaqueness at higher amounts of catalyst. Additionally, after several hours of operation, the reactor volume cannot accommodate the large amount of hydrogen generated from water splitting. Thus, the partial pressure of hydrogen in the reactor vessel would increase, thus increasing the solubility of hydrogen in the reaction solution, which consequently decreases the hydrogen production rates [87].

4.1.7. Recycle studies on bimetallic catalysts

To examine the photostability and recyclability of the bimetal

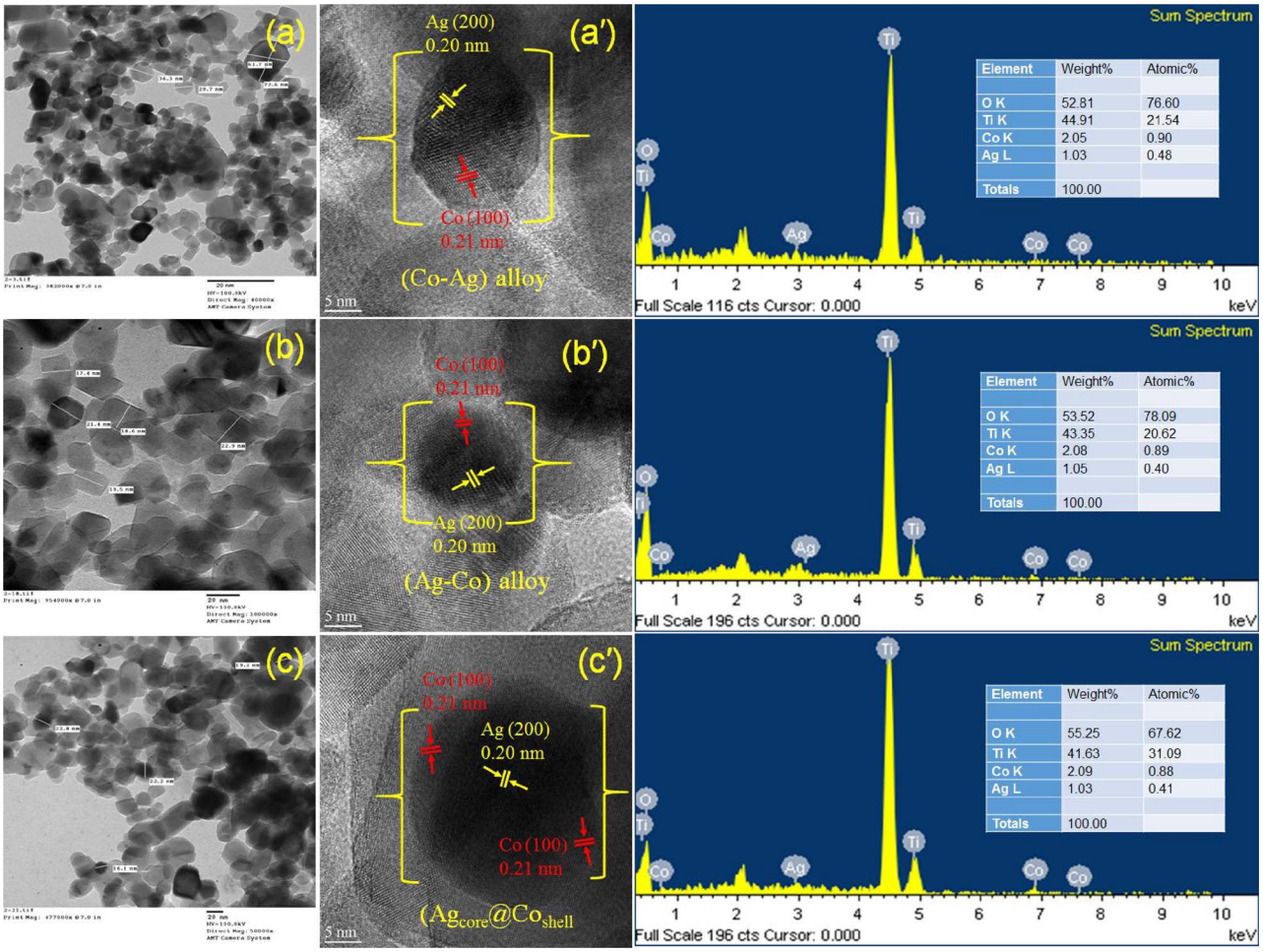

Fig. 10. TEM and EDX images of freshly prepared samples: (a) Co_{loaded}-AgTNP, (b) Ag_{loaded}-CoTNP, and (c) $(Ag\text{-}Co)_{coloaded}$TNP. HRTEM images of post-reaction/used samples: (a′) Co_{loaded}-AgTNP, (b′) Ag_{loaded}-CoTNP, and (c′) $(Ag\text{-}Co)_{coloaded}$TNP.

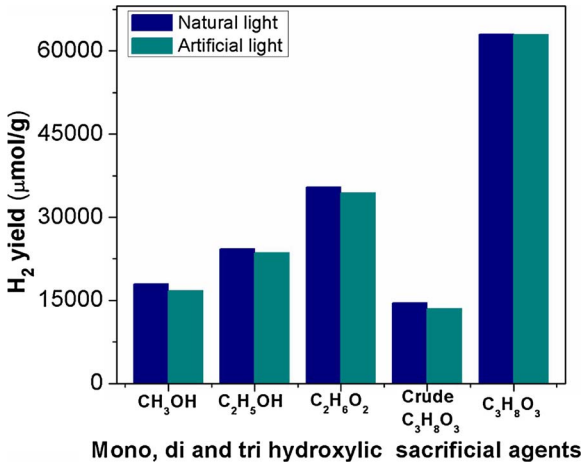

Fig. 11. Photocatalytic activity test for H_2 production with mono-, di-, and tri-hydroxylic sacrificial agents.

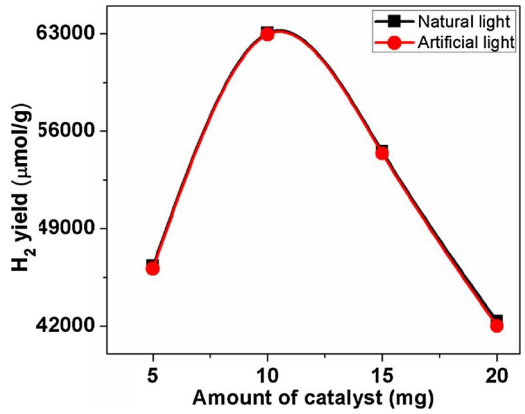

Fig. 12. Amount of photocatalyst over (Ag-Co)$_{coloaded}$TNP on hydrogen production rate.

photocatalyst, Ag$_{loaded}$-CoTNP, Co$_{loaded}$-AgTNP, and (Ag-Co)$_{coloaded}$TNP were employed as a representative sample to conduct five successive photocatalytic reactions (total duration of 20 h). As illustrated in Fig. 13, the samples maintained their high catalytic activity toward the photocatalytic water splitting process with slight reduction in hydrogen production after five successive cycles under the same experimental conditions, signifying a high photostability and reusability. The minor decrease in total hydrogen production was observed after cycle, which can be ascribed to the poor surface interaction of the reaction intermediates formed during glycerol oxidation in solution. These intermediates could have been adsorbed onto the photocatalyst surface, which affected the light penetration to the surface and resulted in a decrease in the rate of hydrogen generation.

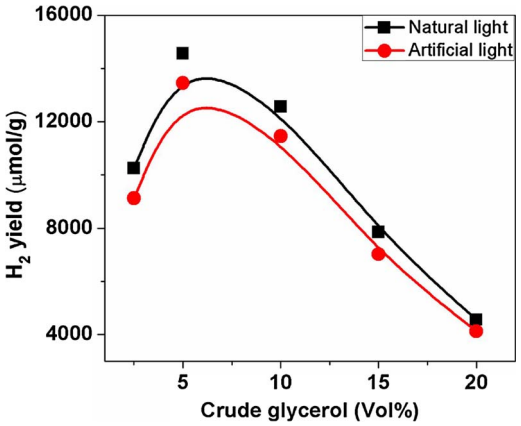

Fig. 14. Effect of crude glycerol concentration on H_2 evolution rates over (Ag-Co)$_{coloaded}$TNP catalyst.

4.1.8. *Effect of crude glycerol concentration*

The effect of biodiesel-derived crude glycerol concentration on hydrogen production activity over the (Ag-Co)$_{coloaded}$TNP catalyst was studied under natural and artificial solar light irradiation and the results are shown in Fig. 14. With increase in crude glycerol concentration up to 5 vol%, the hydrogen production activity increased (14.5 mmol g^{-1}), while above 5 vol% crude glycerol, the rate of hydrogen production gradually decreased. Below 5 vol% crude glycerol concentration, the rate of photocatalytic activity is limited (10.2 mmol g^{-1}), which is envisaged by mass transfer of crude glycerol from solution to the catalyst surface. At a higher crude glycerol concentration (~5 vol%), the reaction medium became less polar and the active sites became saturated due to the high adsorption of crude glycerol and its intermediates, which hindered the catalytic activity [88].

5. Conclusions

The present study demonstrates that alloy/core-shell-type bimetal-loaded TNP exhibits a unique adsorption property that is different from those of the single metal systems due to the electronic modification of the shell metal through its interaction with the core metal and the support. In summary, monometallic and bimetallic photocatalysts were successfully synthesized by the sol-gel and impregnation methods and followed by insitu photoreduction. This method is suitable for the preparation of core-shell NPs and plays a prominent role in the localized SPR effect by absorbing the broad spectrum of visible light. The XRD results revealed the highly crystalline nature of TiO_2 and well-defined characteristic peaks of bimetallic alloy and core-shell NPs for

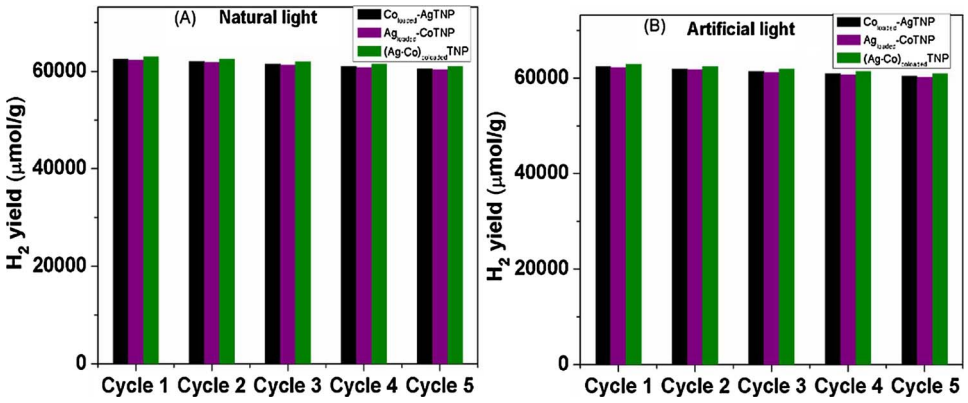

Fig. 13. Photocatalytic recycling activity of Co$_{loaded}$-AgTNP, Ag$_{loaded}$-CoTNP, and (Ag-Co)$_{coloaded}$TNP.

the Ag_{loaded}-CoTNP, Co_{loaded}-AgTNP, and $(Ag\text{-}Co)_{coloaded}$TNP photocatalysts. On the other hand, the UV–vis DRS spectra of Ag@Co NPs loaded on TNP showed a red-shifted SPR peak as well as an increase in the band width compared to that ofAg/Co-loaded TNP. Both the results suggest alloy (formation of single band) and core-shell (formation of two bands) nature of the synthesized Ag@Co-loaded TNP nanoparticles. The shift in the BE in the XPS spectra allowed us to identify the presence of metallic Co/Ag in the post-reaction photocatalysts (formation alloy/core-shell) and Co/Ag oxides in the freshly prepared photocatalysts. H_2-TPR analysis revealed the reduction of monometal and mixed metal oxides, and their hydrogen uptake values given the percentage of reducibility. PL spectra revealed the lower electron-hole recombination rate in the alloy/core-shell-loaded TNP. In addition, HRTEM images clearly showed the formation of alloy and core-shell NPs. The results demonstrated that the optimal $(Ag\text{-}Co)_{coloaded}$TNP sample showed the highest photocatalytic performance, with a noteworthy hydrogen evolution rate of 63 mmol g^{-1} under natural solar light irradiation. The photocatalyst demonstrated a high photostability and recyclability (five successive cycles) for hydrogen production under natural sun light.

Acknowledgements

This work was supported by the Basic Research Science and Technology Projects through the National Research Foundation of Korea Grant funded by the Ministry of Science, ICT & Future Planning (No. 2015R1A1A3A04001268), for which the authors are very grateful.

Appendix A. Supplementary data

Supplementary material related to this article can be found, in the online version, at doi:https://doi.org/10.1016/j.apcatb.2018.03.015.

References

[1] R.D. Cortright, R.R. Davda, J.A. Dumesic, Nature 418 (2002) 964–967.
[2] A. Fujishima, K. Honda, Nature 238 (1972) 37–38.
[3] D. Ravelli, D. Dondi, M. Fagnoni, A. Albini, Chem. Soc. Rev. 38 (2009) 1999–2011.
[4] H.L. Jiang, Q. Xu, J. Mater. Chem. 21 (2011) 13705–13725.
[5] H. Kominami, H. Nishimune, Y. Ohta, Y. Arakawa, T. Inaba, Appl. Catal. B: Environ. 111–112 (2012) 297–302.
[6] J. Zhang, Y. Lu, L. Ge, C. Han, Y. Li, Y. Gao, S. Li, H. Xu, Appl. Catal. B: Environ. 204 (2017) 385–393.
[7] M. Tahir, B. Tahir, N.A.S. Amin, Appl. Catal. B: Environ. 204 (2017) 548–560.
[8] Y. Zhang, N. Zhang, Z.R. Tang, Y.J. Xu, J. Phys. Chem. C 118 (2014) 5299–5308.
[9] Z. Wan, Q. Xu, H. Li, Y. Zhang, Y. Ding, J. Wang, Appl. Catal. B: Environ. 210 (2017) 67–76.
[10] J. Tian, T. Yan, Z. Qiao, L. Wang, W. Li, J. You, B. Huang, Appl. Catal. B: Environ. 209 (2017) 566–578.
[11] A. Watanabe, K. Ikemiya, A. Chikamatsu, Y. Hirose, T. Hasegawa, Chem. Lett. 43 (2014) 225–227.
[12] A. Holewinski, J.C. Idrobo, S. Linic, Nat. Chem. 6 (2014) 828–834.
[13] A.Z. Jurek, J. Nanomater. 2014 (2014) 1–17. Article ID 208920.
[14] Z. Khan, S.A. Al-Thabaiti, A.Y. Obaid, M.A. Malik, T.A. Khan, J. Mol. Liq. 222 (2016) 272–278.
[15] S.M. Kim, Y.G. Jo, M.H. Lee, N. Saito, S.Y. Lee, Electrochim. Acta 233 (2017) 123–133.
[16] J.G. Torres, E. Valles, E. Gomez, J. Nanopart. Res. 12 (2010) 2189–2199.
[17] Z. Parang, A. Keshavarz, S. Farahi, S.M. Elahi, S. Parhoodeh, ScientiaIranica, F. Transactions, Nanotechnology 19 (2012) 943–947.
[18] D. Wang, T. Hisatomi, T. Takata, C. Pan, M. Katayama, J. Kubota, K. Domen, Angew. Chem. Int. Ed. 52 (2013) 11252–11256.
[19] A. Yu, C. Lee, N.S. Lee, M.H. Kim, Y. Lee, ACS Appl. Mater. Interfaces 48 (2016) 32833–32841.
[20] S.S.K. Kamal, J. Vimala, P.K. Sahoo, P. Ghosal, M. Raja, L. Durai, S. Ram, Phys. B 448 (2014) 96–99.
[21] A. Watanabe, Y. Kotake, Y. Kamata, A. Chikamatsu, K. Ueno, H. Misawa, T. Hasegawa, J. Phys. Chem. Lett. 5 (2014) 25–29.
[22] B. Bai, J. Li, ACS Catal. 4 (2014) 2753–2762.
[23] K. Ikemiya, K. Konishi, E. Fujii, T. Kogure, M.K. Gonokami, T. Hasegawa, Opt. Mater. Express 4 (2014) 1564–1573.
[24] K.L. Wustholz, A.I. Henry, J.M. McMahon, R.G. Freeman, N. Valley, M.E. Piotti, M.J. Natan, G.C. Schatz, R.P.V. Duyne, J. Am. Chem. Soc. 132 (2010) 10903–10910.
[25] S.K. Singh, Q. Xu, J. Am. Chem. Soc. 131 (2009) 18032–18033.
[26] H.L. Wang, J.M. Yan, Z.L. Wang, S. IlO, Q. Jiang, J. Mater. Chem. A 1 (2013) 14957–14962.
[27] M.K. Carpenter, T.E. Moylan, R.S. Kukreja, M.H. Atwan, M.M. Tessema, J. Am. Chem. Soc. 134 (2012) 8535–8542.
[28] Y. Wu, S. Cai, D. Wang, W. He, Y. Li, J. Am. Chem. Soc. 134 (2012) 8975–8981.
[29] J. Gu, Y.W. Zhang, F. Tao, Chem. Soc. Rev. 41 (2012) 8050–8065.
[30] C. Zhang, B.Q. Chen, Z.Y. Li, J. Phys. Chem. C 119 (2015) 16836–16845.
[31] M. Kotesh Kumar, K. Bhavani, B. Srinivas, S. Naveen Kumar, M. Sudhakar, G. Naresh, A. Venugopal, Appl. Catal. A: Gen. 515 (2016) 91–100.
[32] M. Kotesh Kumar, K. Bhavani, G. Naresh, B. Srinivas, A. Venugopal, Appl. Catal. B: Environ. 199 (2016) 282–291.
[33] L. Qin, G. Si, X. Li, S.Z. Kang, RSC Adv. 5 (2015) 102593–102598.
[34] H. Zhu, Y. Wu, X. Zhao, H. Wan, L. Yang, J. Hong, Q. Yu, L. Dong, Y. Chen, C. Jian, J. Wei, P. Xu, J. Mol. Catal. A: Chem. 243 (2006) 24–30.
[35] G.A.J. Bastida, J. Rivas, M.A. Lopez-Quintela, A. Gonzalez-Penedo, A. Traverse, Sci. Technol. Adv. Mater. 6 (2014) 411–419.
[36] T. Bala, S.K. Arumugam, R. Pasricha, B.L.V. Prasad, M. Sastry, J. Mater. Chem. 14 (2004) 1057–1061.
[37] E. Iglesias-Silva, J. Rivas, L.M. León Isidro, M.A. López-Quintela, J. Non-Cryst. Solids 353 (2007) 829–831.
[38] M. Mandal, S. Kundu, S.K. Ghosh, S. Panigrahi, T.K. Sau, S.M. Yusuf, T. Pal, J. Colloid Interface Sci. 286 (2005) 187–194.
[39] Z. Xu, Y. Hou, S. Sun, J. Am. Chem. Soc. 129 (2007) 8698–8699.
[40] Y.V. Basova, D.D. Edie, P.Y. Badheka, H.C. Bellam, Carbon 43 (2005) 1533–1545.
[41] W. Zhou, H. Liu, J. Wang, D. Liu, G. Du, J. Cui, ACS Appl. Mater. Interfaces 2 (2010) 2385–2392.
[42] I. Ganesh, A.K. Gupta, P.P. Kumar, P.S. Chandra Sekhar, K. Radha, G. Padmanabham, G. Sundararajan, Mater. Chem. Phys. 135 (2012) 220–234.
[43] Q. Guo, Y. Liu, Appl. Catal. B: Environ. 82 (2008) 19–26.
[44] Y. Liu, Y. Wang, H. Wang, Z. Wu, Catal. Commun. 12 (2011) 1291–1294.
[45] A.Y. Khodakov, W. Chu, P. Fongarland, Chem. Rev. 107 (2007) 1692–1744.
[46] M.M. Yung, E.M. Holmgreen, U.S. Ozkan, J. Catal. 247 (2007) 356–367.
[47] Q. Wang, Y. Peng, J. Fu, G.Z. Kyzas, S.M.R. Billah, S. An, Appl. Catal. B: Environ. 168–169 (2015) 42–50.
[48] A.A. Melvin, K. Illath, T. Das, T. Raja, S. Bhattacharyy, C.S. Gopinath, Nanoscale 7 (2015) 13477–13488.
[49] C. Haung, X. Liu, L. Kong, W. Lan, Q. Su, Y. Wang, Appl. Phys. A 87 (2007) 781–786.
[50] T. Ohsaka, F. Izumi, Y. Fujiki, J. Raman Spectrosc. 7 (1978) 321–324.
[51] S. Sajjad, S.A.K. Leghari, F. Chen, J. Zhang, Chem. Eur. J. 16 (2010) 13795–13804.
[52] J. Navas, A. Sanchez-Coronilla, T. Aguilar, N.C. Hernandez, D.M. de los Santos, J. Sanchez-Marquez, D. Zorrilla, C. Fernandez-Lorenzo, R. Alcantara, J. Martın-Calleja, Phys. Chem. Chem. Phys. 16 (2014) 3835–3845.
[53] M.I. Zaki, A. Katrib, A.I. Muftah, T.C. Jagadale, M. Ikram, S.B. Ogale, Appl. Catal. A 452 (2013) 214–221.
[54] C. Huang, X. Liu, Y. Liu, Y. Wang, Chem. Phys. Lett. 432 (2006) 468–472.
[55] G. Sadanandam, K. Lalitha, V. DurgaKumari, M.V. Shankar, M. Subrahmanyam, Int. J. Hydrogen Energy 38 (2013) 9655–9664.
[56] V.M. Jimenez, J.P. Espinos, A.R. Gonzalez-Elipe, Surf. Interface Anal. 26 (1998) 62–71.
[57] T.J. Chuang, C.R. Brundle, D.W. Rice, Surf. Sci. 59 (1976) 413–429.
[58] N.J.M. Sanghamitra, S. Mazumdar, Langmuir 24 (2008) 3439–3445.
[59] E. Galuri, C. Guldur, S. Srivsnnavit, S. Osuwan, Appl. Catal. A: Gen. 182 (1999) 147–163.
[60] N. Luo, L. Mao, L. Jiang, J. Zhan, Z. Wu, D. Wu, Mater. Lett. 63 (2009) 154–156.
[61] D.H. Ha, L.M. Moreau, S. Honrao, R.G. Hennig, R.D. Robinson, J. Phys. Chem. C 117 (2013) 14303–14312.
[62] G. Preda, G. Pacchioni, Catal. Today 177 (2011) 31–38.
[63] V.R. Stamenkovic, B.S. Mun, M. Arenz, K.J.J. Mayrhofer, C.A. Lucas, G. Wang, P.N. Ross, N.M. Markovic, Nat. Mater. 6 (2007) 241–247.
[64] X. Sun, W. Dai, G. Wu, L. Li, N. Guan, M. Hunger, Chem. Commun. 51 (2015) 13779–13782.
[65] K.H. Leong, B.L. Gan, S. Ibrahim, P. Saravanan, Appl. Surf. Sci. 319 (2014) 128–135.
[66] V. Vamathevan, R. Amal, D. Beydoun, G. Low, S. McEvoy, J. Photochem. Photobiol. A 148 (2002) 233–245.
[67] Y. Shiraishi, H. Sakamoto, Y. Sugano, S. Ichikawa, T. Hirai, ACS Nano 7 (2014) 9287–9297.
[68] L.M. Liz-Marzán, Langmuir 22 (1) (2006) 32–41.
[69] A. Henglein, J. Phys. Chem. 97 (1993) 5457–5471.
[70] J. Singh, K. Sahu, A. Pandey, M. Kumar, T. Ghosh, B. Satpati, T. Som, S. Varma, D.K. Avasthi, S. Mohapatr, Appl. Surf. Sci. 411 (2017) 347–354.
[71] J. Li, Cy. Liu, Z. Xie, Mater. Res. Bull. 46 (2011) 743–747.
[72] P. Mulvaney, Langmuir 12 (1996) 788–800.
[73] S.W. Verbruggena, M. Keulemans, M. Filippousi, D. Flahaut, G.V. Tendeloo, S. Lacombe, J.A. Martens, S. Lenaerts, Appl. Catal. B: Environ. 156–157 (2014) 116–121.
[74] A.K. Singh, Q. Xu, ChemCatChem 5 (2013) 652–676.
[75] J.H. Sinfelt, G.H. Via, F.W. Lytle, J. Chem. Phys. 72 (1980) 4832–4844.
[76] G.M. Nunez, A.J. Rouco, J. Catal. 111 (1988) 41–49.
[77] K. Asakura, Y. Iwasawa, M. Yamada, J. Chem. Soc. Faraday Trans. 84 (1) (1988) 2457–2464.
[78] R. Baba, S. Nakabayashi, A. Fujishima, K. Honda, J. Am. Chem. Soc. 109 (1987) 2273–2277.
[79] H. Tada, K. Teranishi, S. Ito, H. Kobayashi, S. Kitagawa, Langmuir 16 (2000) 6077–6080.

[80] J. Yu, Y. Hai, B. Cheng, J. Phys. Chem. C 115 (2011) 4953–4958.
[81] D.I. Kondarides, V.M. Daskalaki, A. Patsoura, X.E. Verykios, Catal. Lett. 122 (2008) 26–32.
[82] Y.Z. Yang, C.H. Chang, H. Idriss, Appl. Catal. B: Environ. 67 (2006) 217–222.
[83] K. Lalitha, G. Sadanandam, V. DurgaKumari, M. Subrahmanyam, B. Sreedhar, N.Y. Hebalkar, J. Phys. Chem. C 114 (2010) 22181–22189.
[84] N. Strataki, V. Bekiari, D.I. Kondarides, P. Liano, Appl. Catal. B: Environ. 77 (2007) 184–189.
[85] V.M. Daskalaki, D.I. Kondarides, Catal. Today 144 (2009) 75–80.
[86] G. Wu, T. Chen, W. Su, G. Zhou, X. Zong, Z. Lei, Int. J. Hydrogen Energy 33 (2008) 1243–1251.
[87] W.Y. Cheng, T.H. Yu, K.J. Chao, S.Y. Lu, ChemCatChem 6 (2014) 293–300.
[88] D.W. Skaf, N.G. Natrin, K.C. Brodwater, C.R. Bongo, Catal. Lett. 142 (2012) 1175–1179.